Atmos. Chem. Phys. Discuss., 9, 18545–18596, 2009
www.atmos-chem-phys-discuss.net/9/18545/2009/

Atmospheric Chemistry and Physics Discussions

This discussion paper is/has been under review for the journal *Atmospheric Chemistry and Physics (ACP)*. Please refer to the corresponding final paper in *ACP* if available.

Lagrangian mixing in an axisymmetric hurricane model

B. Rutherford[1], **G. Dangelmayr**[1], **J. Persing**[1], **M. Kirby**[1], **and M.T. Montgomery**[2]

[1]Department of Mathematics, Colorado State University, Fort Collins, CO 80523-1874, USA
[2]Department of Meteorology, Naval Postgraduate School, Monterey, CA 93943-5114, USA

Received: 23 July 2009 – Accepted: 10 August 2009 – Published: 9 September 2009

Correspondence to: B. Rutherford (rutherfo@math.colostate.edu)

Published by Copernicus Publications on behalf of the European Geosciences Union.

Abstract

This paper discusses the extension of established Lagrangian mixing measures to make them applicable to data extracted from a 2-D axisymmetric hurricane simulation. Because of the non-steady and unbounded characteristics of the simulation, the previous measures are extended to a moving frame approach to create time-dependent mixing rates that are dependent upon the initial time of particle integration, and are computed for nonlocal regions. The global measures of mixing derived from finite-time Lyapunov exponents, relative dispersion, and a measured mixing rate are applied to distinct regions representing different characteristic feautures within the model. It is shown that these time-dependent mixing rates exhibit correlations with maximal tangential winds during a quasi-steady state, establishing a connection between mixing and hurricane intensity.

1 Introduction

The question of the interaction between different characteristic regions of a hurricane, in particular the eye, eyewall, and environment, is considered of fundamental importance in the study of structure and intensity (Frank and Ritchie, 1999, 2001; Kossin and Eastin, 2001; Kossin and Schubert, 2001; Schubert et al., 1999; Willoughby, 2001). In particular, mixing in the lower troposphere at the eye-eyewall interface (Cram et al., 2007; Montgomery et al., 2006; Persing and Montgomery, 2003) has been proposed to play an important role for intensification. The proposed mechanisms are either direct and mechanical or indirect and thermodynamic. Direct and mechanical mechanisms reduce intensity as air with low absolute angular momentum from the eye is stirred to the radius of maximum winds (RMW). Indirect and thermodynamic mechanisms stir air with high entropy from the eye to the eyewall that will generate enhanced local buoyancy (Smith et al., 2005; Braun, 2002; Liu et al., 2002) leading to an enhanced energetic cycle for the hurricane as a whole (e.g. as a modified heat cycle). Maximum

ACPD

9, 18545–18596, 2009

tangential winds (found in the eyewall generally at $z \approx 1$ km) will be used here as the principal measure of intensity.

Mixing in hurricanes is often viewed in an Eulerian manner, based on the instantaneous velocity fields. If the velocity fields are time varying, the Eulerian structures may not be representative of the actual particle motion. In recent work in fluid dynamics, time-dependent Lagrangian hyperbolic invariant manifolds have been studied that partition the domain into distinct regions and are visualized as ridges of Lagrangian scalar fields (Haller, 2000, 2002; Haller and Poje, 1997; Haller and Yuan, 2000), see Rutherford et al. (2009) for a recent application to a 2-D hurricane-like vortex model. Most of these studies are for time-varying 2-D velocity fields in closed and bounded domains. An extension of the use of these methods to the 3-D case is given in Green et al. (2006). In this paper we investigate a 2-D flow that is more complicated because the domain is unbounded and there is an inflow and outflow. Lagrangian structures associated with boundaries have been identified in Haller (2004); Surana and Haller (2007), and generally differ from the Eulerian separation points.

Statistical measures of Lagrangian mixing have been applied to 2-D fluid models (Voth et al., 2003; Antonsen Jr. et al., 1996), but the mixing characteristics are time-dependent only in the sense that they vary with the integration time. While this is sufficient for steady or periodic velocity fields, in general time-varying velocity fields there is also a significant dependence on the initial time at which the trajectories are seeded. This holds for all statistical measures used so far, including relative dispersion, which has been used to diagnose atmospheric mixing (Huber et al., 2001) in a limited way in a global circulation problem.

In this paper we apply Lagrangian techniques to study mixing in the axisymmetric hurricane model of Rotunno and Emanuel (1987). The model of the hurricane shows the principal structures of 3-D hurricanes (e.g. eye, eyewall updraft, near-surface inflow, and outflow jet), while resolving the 2-D velocity fields in the radial and vertical directions. The advantages of axisymmetric models are that the size of the problem is reduced and the geometry is simpler. The structures found to be characteristic for the

ACPD
9, 18545–18596, 2009

mixing processes within an axisymmetric model may, with caution, be extended to give clues about mixing within 3-D models or reality. The model of Rotunno and Emanuel (1987) yields time-dependent 2-D velocity fields that are very complex spatially and temporally about a quasi-steady state. Many dynamically interesting structures arise which are also time dependent. The fluid is not incompressible, and the domain is unbounded, which present a challenge to many current mixing techniques. The temporal complexity of the velocity fields makes the extraction of coherent structures difficult, as structures may have very short times of existence.

Given the complexity and time-dependent nature of the velocity field in the Rotunno and Emanuel model, it is neccessary to develop a hybrid (local-global) approach to measuring mixing rates. Local properties of flow structures are generally not valuable for characterizing the entire flow because the time-dependent nature averages out any local effects. However, global measures of mixing are not suitable for this model either, because much of the mixing occurs around the eyewall updraft region, which is where the maximum winds occur. Outer environment and eye behavior are very separate processes from the mixing that occurs in and around the updraft, hence diagnosing the mixing for the entire domain from a single measure is not reasonable. Most current methods are either local or global. The local methods study particular features such as hyperbolic trajectories and their stable and unstable manifolds, and track the effects of these features. Global measures attempt to define a rate of mixing that is representative of the entire system. In the axisymmetric hurricane model used in this study, the strong time dependence makes local structures disappear or bifurcate after several minutes, and their mixing properties are lost. Global measures are difficult to employ because the domain has many distinct mixing regions that do not completely interact with all of the other regions. To diagnose mixing in a domain that has distinct mixing regions, we adapt both local and global mixing diagnostics to nonlocal regions. The nonlocality of the regions requires extracting mixing measures from ensembles of trajectories, which makes these measures statistical in nature.

ACPD
9, 18545–18596, 2009

Our approach to solving the hurricane mixing problem will be guided by considering time and space dependence of mixing processes. The dynamically distinct regions of hurricanes (e.g. the eye, the eyewall, environment, etc.) require that the space dependence of mixing properties follows a regional approach. The domain is partitioned into regions, and a mixing rate is calculated for each region, giving a spatial dependence to the mixing rates. For general time dependence, not only variations in the integration time, but also variations in the initial time have to be used to define the mixing rates. The result is a time series of mixing rates computed for each spatial region. The initial time-dependent mixing rates are then compared with measures of intensity to establish correlations between these characteristic quantities. The correlation analysis shows that the mixing rates computed for some of the regions are sigificantly correlated with the maximum tangential winds.

A mixing rate is a measure of how quickly an initial tracer in a fluid becomes homogenized. The homogenization process has been studied for autonomous or time-periodic velocity fields in bounded and closed domains, and gives a mixing rate for the entire system. This rate can be compared to other rates derived from measures of advection or diffusion. The time dependence of the axisymmetric model makes diffusion very difficult to measure because the filimentation that occurs with a diffusive process undergoes bifurcations as soon as the filiments develop. Advective measures of mixing converge fast in integration time making them more suitable for this model. Since this follows from particle trajectories, the associated mixing rates are Lagrangian in nature, and measure the interaction of features that move with the flow.

The outline of the paper is as follows. Section 2 gives an overview of current Lagrangian mixing rates. In Sect. 3 we describe the characteristics of the axisymmetric model that is used for this study. The adaptation of current methods to make them applicable to our non-steady and open fluid-flow problem, along with the numerical methods used is described in Sect. 4. The results of our study are presented in Sects. 5–8. In Sect. 5 we show and discuss the Lagrangian scalar fields. Section 6 gives a Lagrangian characterization of the eye-eyewall interaction, and Sect. 7 shows how the Lagrangian

ACPD
9, 18545–18596, 2009

structures are related to low and high intensity steady state approximations. In Sect. 8, we analyze correlations between measures of intensity and mixing rates. A discussion and conclusions are given in Sect. 9.

2 Overview of current Lagrangian methods

Lagrangian mixing measures have advantages over Eulerian measures for their applicability to time dependent fluid flows. For time dependent flows, trajectories may cross Eularian boundaries, and diverge from instantaneous features of the flow. Lagrangian techniques capture the total separation of trajectories and provide structures that are invariant under the flow. The current methods can generally be classified as either local or global. The local techniques quantify the local rate of stretching of an initial area element. Places with the highest stretching give time dependent manifolds, which are invariant and determine the local transport properties by following the manifolds through the flow. These techniques are useful for incompressible flows where the velocity field varies slowly both in space and time. Some of the local techniques currently in use are finite-time Lyapunov exponents (FTLE's) (Haller, 2002; Haller and Poje, 1997; Haller and Yuan, 2000), distinguished hyperbolic trajectories, finite size Lyapunov exponents (FSLE's) (Green et al., 2006), and relative dispersion (Huber et al., 2001).

Global Lagrangian techniques provide representative mixing characteristics of an entire domain, without exact extraction of structures, and are statistical in nature. Global mixing measures have been applied to flows in bounded domains with no dominant flow characteristics, and with with no general time dependence. The global measures are related to the homogenization of a tracer within the domain, and are usually extensions of local measures to the entire domain. The measured mixing rate determines how fast the tracer is homogenized (Voth et al., 2003). Another global mixing rate is defined through the distribution of FTLE values and is an extension of the local measure of advection to the entire domain.

ACPD
9, 18545–18596, 2009

2.1 Measured mixing rate (MMR)

The mixing rate of a system can be measured by calculating the rate at which an initial tracer becomes homogenized by the flow. If an initial tracer is planted uniformly over a subdomain at time t_0 and evolved, then the variance of the tracer concentration should decay over time as the tracer fills the entire domain. If $C\ (t, t_0, \mathbf{x})$ is the concentraton of the tracer at time t initiated at time t_0, then the variance $\sigma_C(t, t_0)$ of C should decay exponentially over time and thus can be modeled by

$$\sigma_C(t, t_0) = A_0 e^{-r|t-t_0|} + A_1. \quad (1)$$

The relaxation constant r is called the measured mixing rate (MMR) (Voth et al., 2003). It is assumed here that r is representative of the entire system, and the initial tracer profile is not important in a long enough integration time, since the positions of fluid particles in a closed domain eventually become indistinguishable with respect to their initial conditions. For the non-autonomous axisymmetric model, we make this rate space and time dependent by varying the initial spatial region A in which trajectories are seeded, as well as the initial time t_0.

For A we choose regions in the eye, eyewall updraft, and the boundary layer inflow, which are representative of particular features of the flow. These regions have very different mixing properties, and different associated mixing rates. Since the fluid in this model does not eventually become homogenized, the mixing rate is a measure of how trajectories characteristic of a certain feature disperse, e.g. become advected through a jet. Trajectories that enter the eyewall updraft exit the domain through the upper level outflow jet, so there are many trajectories that exit the domain in finite time, and there are large regions of the domain that trajectories from the core will not enter. To accomodate this trajectory behavior, a finite-time version of the mixing rate is used here. Trajectories are advected for an integration time such that they remain within the spatial domain. The mixing rate $r(A, t_0)$ then approximates the long time scalar variance decay by the homogenization over a short time. We note that for flows that do not eventually reach a homogenized state, the *degree* of homogenization, A_1, can be a

ACPD
9, 18545–18596, 2009

relevant measure of mixing. This measure is different from the *rate r* of homogenization in that it measures how clustered the set remains as it is advected.

2.2 Finite time Lyapunov exponents (FTLE's) and Lagrangian coherent structures (LCS's)

Lagrangian coherent structures (LCS's) are finite-time invariant manifolds which are advected by the flow. Particle trajectories do not cross LCSs, but diverge from them exponentially in the direction orthogonal to the LCS. LCS's are determined from the rate of maximal expansion of nearby trajectories. A scalar measure of maximal stretching is provided by the field of finite-time Lyapunov exponents (FTLE's) (Shadden et al., 2005). Let

$$\mathbf{x}_0 \mapsto \phi_{t_0}^{t}(\mathbf{x_0}) \tag{2}$$

be the flow map from time t_0 to time t associated with a 2-D non-steady velocity field $\mathbf{v}(\mathbf{x}, t)$, that is, the solution of $\dot{\mathbf{x}}=\mathbf{v}(\mathbf{x}, t)$ with initial condition $\mathbf{x}(t_0)=\mathbf{x}_0$. Consider an infinitesimal perturbation $\mathbf{x}'_0$ of the point $\mathbf{x}_0$. After a time T, the perturbation becomes

$$\mathbf{x}'(t_0+T) = \phi_{t_0}^{t_0+T}(\mathbf{x_0}+\mathbf{x}'_0)-\phi_{t_0}^{t_0+T}(\mathbf{x}_0) \tag{3}$$

$$= \frac{d\phi_{t_0}^{t_0+T}(\mathbf{x}_0)}{d\mathbf{x}_0}\mathbf{x}'_0+\mathcal{O}(\left\|\mathbf{x}'_0\right\|^2). \tag{4}$$

To find the magnitude of the growth rate of the perturbation, we drop the $\mathcal{O}(\left\|\mathbf{x}'_0\right\|^2)$ term and take the Euclidean norm

$$\|\mathbf{x}'(t)\| = \sqrt{\langle \mathbf{x}_0, \Delta\mathbf{x}'_0)\rangle} \tag{5}$$

where the matrix

$$\Delta = \frac{d\phi_{t_0}^{t_0+T}(\mathbf{x_0})^*}{d\mathbf{x_0}}\frac{d\phi_{t_0}^{t_0+T}(\mathbf{x}_0)}{d\mathbf{x_0}} \tag{6}$$

ACPD
9, 18545–18596, 2009

(the asterik denotes the transpose of a matrix or vector) is symmetric and gives a finite time representation of the Cauchy-Green deformation tensor. The maximal expansion occurs when $\mathbf{x}_0'$ is aligned with the eigenvector corresponding to the largest eigenvalue, $\lambda_{\max}(\Delta)$, of Δ,

$$\max_{\|\mathbf{x}_0'\|} = \epsilon \|\mathbf{x}'(T)\| = \sqrt{\lambda_{\max}(\Delta)}\epsilon = \exp\left(\sigma_{t_0}^{t_0+T}(\mathbf{x}_0)|T|\right)\epsilon,$$

where

$$\sigma_{t_0}^{t_0+T}(\mathbf{x}_0) = \frac{1}{2|T|}\log\lambda_{\max}(\Delta) \tag{7}$$

is the largest finite time Lyapunov exponent for the integration time T at the point $\mathbf{x}_0$ at time t_0. The FTLE is computed forward ($T>0$) and backward ($T<0$) in time, which allows detection of forward-time repelling and attracting material lines.

An initial grid of seeded trajectories can be advected to give a scalar field of FTLE values dependent on initial-time. High FTLE values correspond to large separation or trajectories. Ridges of FTLE fields are defined as LCSs (Shadden et al., 2005), and form a framework for mixing. The extraction of ridges from a time varying FTLE-field is impractical, but the structures are often obvious from visual inspection.

While the exact extraction of LCSs is generally not possible, FTLEs still give the total separation of trajectories within a region, and the statistical distribution of FTLE-values allows definition of global mixing rates. Antonsen Jr. et al. (1996) have shown that for autonomous or time-periodic velocity fields in closed and bounded domains, the variance of a tracer coincides with the quantity

$$G(t,t_0) = \int \sigma^{(1/2)} e^{-\sigma t} P(\sigma,t)\,d\sigma, \tag{8}$$

where $P(\sigma, t)$ is the probability distribution function of the FTLE values. For non-steady velocity fields in open domains this coincidence cannot be expected, but still the function $G(t)$ should show a similar exponential decay like the tracer variance. Thus, assuming that $G(t)$ has the form

$$G(t) = A'_0 e^{-R|t-t_0|} + A'_1, \quad (9)$$

we can solve numerically for R to obtain a predicted FTLE mixing rate (FMR). This rate is meant to measure the advective mixing processes and does not account for the diffusive processes that govern the long time mixing. For short integration times, advection dominates diffusion, and the mixing rate from FTLE values gives a good measure of mixing. Since the exponential decay form describes the aymptotic behavior of $G(t)$ for large $|t - t_0|$ this measure is not useful for very short integration times. The integration time must be chosen long enough that LCSs become resolved, but short enough that excessive filimentation of the structures does not occur. Bifurcations of the LCSs may also limit the practical integration time.

This method is designed for closed bounded domains and steady or time-periodic velocity fields, see Voth et al. (2003) for an application to a time-periodic velocity field with chaotic trajectories. Since the axisymmetric model has general time dependence, and important mixing properties are localized in time and space, we adapt this measure to include initial time dependence and initial space dependence. The resulting time series of mixing rates are then compared to the time series of the measured mixing rates, and to measures of intensity.

2.3 Relative dispersion (RD)

Relative dispersion is based on the average displacement of an ensemble of initially proximate trajectories from a mean particle position (Huber et al., 2001). When an ensemble is taken to be a well defined set of trajectories, relative dispersion can differentiate between sets of initial conditions that have different mixing properties. For

a set A with an ensemble of initial conditions $\mathbf{x}_0 \in A$, the root mean squared (RMS) displacement of the ensemble of trajectories seeded at time t_0 in A is defined as

$$\sigma(t) = \langle \|\mathbf{x}(t) - \overline{\mathbf{x}}(t)\|^2 \rangle^{\frac{1}{2}}, \tag{10}$$

where $\langle . \rangle$ denotes the average over the set, and $\overline{\mathbf{x}}$ is the mean particle position. The relative dispersion $K(t)$ is defined by

$$K(t) = \frac{1}{2}\frac{d}{dt}\sigma^2(t), \tag{11}$$

and $\sigma(t)$ has a power law relationship for $t \rightarrow t_0$ Huber et al. (2001).

$$\sigma(t) \propto |t - t_0|^{\gamma}. \tag{12}$$

Values of γ above 0.5 are defined as superdiffusive and indicate that trajectories are carried quickly by a jet or across a line of high shear. Values below 0.5 are defined as subdiffusive. For an initial set the relative dispersion is dependent on the time scales at which mixing occurs. For a given integration time $T = t - t_0$, we consider the relative dispersion (RD) as a function of an initial set A, and the initial time t_0, $K(A, t_0)$.

2.4 Relative dispersion from FTLE's (FRD)

While FTLEs and relative dispersion are similar measures of trajectory separation, the FMR is not directly comparable to the RD in their given forms. To allow a comparison between the FTLE mixing rate and relative dispersion, we define the RMS displacement of an ensemble of trajectories in the direction of maximal expansion through the FTLE values by

$$D^t_{t_0}(A) = \left\langle \exp 2\sigma^t_{t_0}(\mathbf{x})|t - t_0| \right\rangle^{1/2} \tag{13}$$

$$\propto |t - t_0|^{\gamma'}, \tag{14}$$

ACPD
9, 18545–18596, 2009

which gives a power γ' for $t \to t_0$. The FTLE based relative dispersion (FRD) is then defined by

$$K_f(t) = \frac{1}{2}\frac{dD^2}{dt}(t), \tag{15}$$

and is, for the integration time $T = t - t_0$, considered as a function of A and t_0, similar to the RD. The FRD can be considered as an average stretching factor for an ensemble of trajectories. For comparing t_0-dependent time series, we normalize their L_2-norms to unity.

3 Model overview

The axisymmetric, nonhydrostatic, cloud-resolving hurricane model of Rotunno and Emanuel (1987) is integrated on a staggered C grid using a fixed radial (3.75 km) and fixed vertical (312.5 m) grid spacing at one-fourth the originally published grid spacing. Ice physics are not simulated and explicit convection is employed using a fixed precipitation fall speed of 7 ms^{-1}. Subgrid-scale turbulence is parameterized using a modified Smagorinsky (1963) formulation with horizontal mixing length of 750 m. Radiation is simply represented by Newtonian relaxation to the initial basic state potential temperature profile with a cooling rate capped at 2 K day^{-1}. A sponge layer is provided above the model tropopause. Surface fluxes of momentum and enthalpy are conducted with a bulk aerodynamic formulation with the ratio of drag and enthalpy coefficients set to unity and the drag allowed to vary with wind speed by Deacon's formula (Roll, 1965). The initial sounding is that of 4× run by Persing and Montgomery (2003). Data output is at a two-minute interval starting with a time (day 13) when a quasi-steady intensity ($\approx$85 m s^{-1}) is reached for the simulation.

The (u,w)-flow (in the radial/vertical plane of motion) (Fig. 1) has several dominant characteristics which are often separated by lines of high shearing. The main feature is the axisymmetric eyewall. It appears as a slanted, vertically oriented structure that

ACPD
9, 18545–18596, 2009

separates from the sea surface at approximately r=20 km, and goes upward to a maximum height of z=15 km. Inside of the eyewall is the eye which has very slow velocities. The eyewall updraft takes trajectories upward and is separated from the eye by a line of high vertical shearing. The boundary layer inflow is the main source of material that enters into the updraft. As material moves through the updraft, it enters the upper level outflow, where it goes outward and leaves the domain. There is also a midlevel inflow that brings material inward. This inflow is not as strong as the boundary layer inflow, and trajectories that enter through this inflow mix into the updraft through hyperbolic processes.

The model gives strong time dependent velocity fields, even in a relatively steady state of intensity, leading to different structures for different initial times. The presence of a secondary convective region outside of the main updraft changes the invariant structures that define the updraft, and is important for a change in the eyewall-environment flux.

4 Numerical methods

Mixing rates are computed by adapting the techniques from Sect. 2 to seeded sets of trajectories. Trajectories are advected in radius and height through a fourth order Runge-Kutta method. Since initial conditions do not become eventually homogenized throughout the entire domain, and because trajectories leave the domain, the initial conditions for trajectories become important.

Trajectories are seeded into initial boxes, which are representative regions for different aspects of the flow (Fig. 2). The boxes are placed in the low level inner core region of the hurricane. The boxes approximately split the eye and eyewall updraft, with two boxes in the vertical direction used to distinguish boundary layer properties from other low level properties. The split between the eye and eyewall updraft boxes in the radial direction is placed at the approximate location of the 1 m/s vertical wind contour. Two additional boxes are placed outside the eyewall to capture the processes

ACPD
9, 18545–18596, 2009

in the boundary layer inflow for the lower box, and hyperbolic convective processes in the environment for the upper box.

Trajectories are seeded in the initial boxes at a resolution of 16 times model resolution in the radial direction and 2 times in the vertical direction, giving 320 by 50 total trajectories for each box. The same resolution of trajectories is used for the computation of the FTLE fields, which gives a balance between clear ridges and computational expense.

The MMR requires the computation of a concentration function, which is measured for a given box as the ratio of the number of trajectories in the box at a given time divided by the total number of initial trajectories starting in the given seed box. For counting the number of final trajectories, we have divided the entire domain into a 8 vertical by 20 horizontal grid of boxes of the same size as the six representative boxes. The variance is then computed from the concentrations in all final boxes.

For an initial time, the mixing rates from the concentration and from FTLE fields both follow an exponential decay as a function of integration time (Fig. 3). The mixing rate limit A_1 is determined by taking the minimum concentration variance over the finite integration time, and the initial value A_0+A_1 is the initial variance. The measured mixing rate r is found by taking the log of the time-series $G(t)$ and finding the slope of the linear function using a linear least-squares best fit. For the FMR, the initial value A_0 is determined by the initial FTLE distribution, while the limit A_1 is again determined by taking the minimum value over the integration times. The mixing rate R is determined in the same manner as the MMR.

The relative dispersion $K(t, t_0, A)$ is computed for the initial sets given by the six initial boxes, where the initial and final average positions are the average initial and final positions of the set of trajectories. Because of the aspect ratio of the atmosphere, radial dispersion will factor more strongly into the K measure than vertical dispersion. The FRD is computed from the FTLE values in the six initial boxes to compute an effective RMS displacement. The initial time is varied to create time series to compare with the other computed time series and the maximum winds (shown below). The

ACPD
9, 18545–18596, 2009

integration time is also varied to view the short and long time aspects of the dispersion.

5 Lagrangian fields

The FTLE fields were calculated for a variety of integration times to capture short and long time mixing processes. A longer integration time resolves the manifolds further, but can result in a loss of hyperbolicity or trajectories exiting the domain. The FTLE fields quickly show trajectory separation, and define the eye-eyewall boundary by a line of high FTLE values (Figs. 4–7). The FTLEs provide a one dimensional representation of the stretching, so they do not differentiate between hyperbolic material lines and lines of high shear. Trajectories originating in the eyewall updraft reach a radius of 140 km in the outflow in 120 min, where the outflow jet[1] governs the mixing, and the low level effects cannot be seen. The net effects of advection can still be seen over a longer time scale, which makes a longer integration time useful for determining mixing rates, but local structures become unresolved (Fig. 8).

As integration time is increased (Fig. 8), LCS's should become more resolved, and lengthen. The strong time dependence of the velocity field makes it difficult for any structure to persist over a long integration time, even though the structures may persist over a series of shorter integration times. Advection occurs on a short time scale, but the filamentation of the manifolds is not long enough for diffusion to be noticable. With an integration time of over 20 min, bifurcations of ridges begin to occur very rapidly. At a 120 min integration time, the ridge that governs the short time advection is no longer noticible, but has bifurcated into many ridges. The bifurcations arise from a loss of stability in the hyperbolic trajectory associated with the LCS, as seen by nearby hyperbolic stagnation points that disappear or switch to parabolic or elliptic stability. Lines of high shear reside in parabolic sets, and are characterized by a zero eigenvalue of the flow

[1]The cores of jets show as low mixing regions (blue) as there is very little relative advection of neighboring trajectories there. Jets are bounded by high shear regions, which lead to large relative advection (red) and large FTLE values.

ACPD
9, 18545–18596, 2009

gradient, while hyperbolic material lines have eigenvalues of opposite signs. Numerically, zero eigenvalues are rare, but may oscillate between a small negative and small positive eigenvalue, resulting in bifurcations. Dominant flow features such as inflow, outflow and updraft jets govern much of the trajectory movement. High separation often occurs when nearby trajectories split and one enters a jet. LCS's that are strongly hyperbolic cannot exist near a dominant jet, making shearing LCS's vital for characterizing mixing. Fast trajectory flights enable shearing LCS's to be resolved more quickly than hyperbolic LCS's, promoting a shorter integration time.

6 Eye-eyewall interaction

The Eulerian eye-eyewall boundary at low-levels can be found by looking at the spatial location that separates the strong upward motion of the eyewall from the weak vertical motion of the eye, e.g. a representative contour of the vertical velocity field. The large variation in the velocity field in space and time make the Eulerian eyewall view discontinuous in time. The Lagrangian eyewall view defines the eye-eyewall boundary as the place where there is greatest separation of trajectories, with neighboring trajectories residing in the slow velocity region of the eye and the fast velocity region of the eyewall (Fig. 9). Trajectories in the eye have little movement relative to the LCS, while trajectories in the updraft have movement that is transverse to the LCS.

At an integration time of 20 min, the backward time FTLE field shows an LCS that separates from the sea surface boundary at about r=15 km (Figs. 10 and 11). Though the LCS is found from only a 20 min integration time, it persists for much longer times, and is viewable for the complete analysis period of quasi-steady intensity. Since trajectories in the eyewall updraft run transverse to the LCS, the ridge is easily seen as Lagrangian with nearby trajectories quickly leaving the LCS. The backward time FTLE field gives an attracting LCS. The trajectories that are attracted to the LCS originate in the boundary layer inflow and flow toward the eye. As trajectories attract to the LCS at the eye-eyewall boundary, they are carried into the updraft, where they are no longer

ACPD
9, 18545–18596, 2009

influenced by the attraction properties of the LCS. A 20 min integration produces an LCS that is invariant for a 60 min integration of trajectories. After 60 min, the trajectories have left the region, making the LCS effectively invariant over any integration time.

The LCS consistently separates from the sea-surface at a radius of 15 km, and has nearly the same slope radially outward over all initial times. An Eulerian 1 m/s wind contour changes profile at different times, and may be aligned along or across the LCS (Figs. 10–13). Seeding trajectories along the LCS indicates that trajectories travel transverse to the LCS without crossing, but may cross the Eulerian wind contour.

7 Steady state approximations

The velocity fields reside in a quasi-steady state for a period of several hours, between about 400–800 min. During this time period of 400 min the maximum tangential winds remain in a range of 75 to 88 m/s, where they oscillate rapidly, but in an aperiodic nature. Aside from the differences in intensity, the velocity fields show structural differences in the periods of high maximum tangential winds and lower maximum tangential winds.

The Eulerian velocity field can be used to identify markers, such as instantaneous stagnation points marking hyperbolic trajectories, that give an indication of structures that may exist within the Lagrangian velocity field. We compute two composite-averaged velocity fields from the quasi-steady state period, referred to as strong and weak composites (Fig. 14), which are representative of the phases with strong and weak maximum tangential winds, respectively. The strong (weak) composite is computed by averaging over the instantaneous velocity fields that generate maximum tangential winds at the highest 80% (lowest 20%) of maximum tangential winds over the time interval of 400–800 min. The vertical component of the strong composite shows a single strong updraft, while the vertical wind field of the weak composite shows a dual updraft structure, but with weaker updraft velocities. The radial velocity fields show a

ACPD
9, 18545–18596, 2009

more defined outflow jet for the strong composite.

The composite fields can be considered as autonomous velocity fields. The forward and backward FTLE fields for an autonomous velocity field correspond to finite-time versions of the unstable and stable manifolds of hyperbolic fixed points. The structures are shorter in length than the true stable and unstable manifolds, but they are invariant over the short integration time. Since the velocity field maintains high or low velocities for only a few minutes, invariant structures can only be resolved over a similarly short integration time. Short time structures of the autonomous velocity field can be viewed as markers for finite-time coherent structures of the full velocity fields. The manifolds of the composite velocity fields yield very different structures, not only in the size of the FTLE values, but also in the location and orientation (Figs. 15 and 16). The outflow jet takes a straighter path in the strong composite FTLE field. At the boundary layer, the weak composite FTLE field shows high values where the boundary layer inflow meets the eyewall updraft, allowing fewer trajectories to enter the eyewall. The secondary updraft at 35 km takes some of the boundary layer trajectories, and moves them upward into the region just outside of the eyewall, before a downdraft takes them inward to the eyewall updraft.

Mixing rates for the composite fields (Tables 1 and 2) provide a comparison of the mixing in our six initial seed boxes, and for weak and strong maximum tangential winds. All of the mixing rates are generally higher for the strong composite field, showing that higher intensity coincides with greater mixing. The FMR and MMR are comparable and are generally within a factor of two from each other, with higher values of the MMR except for the low-level eye and low-level eyewall regions. The FRD and RD are comparable, with the FRD giving higher values in the boundary-layer inflow region due to the presence of a series of LCSs that cause trajectories to be transported into the eyewall updraft, or recirculation within an eddy that forms during low velocity times in the environment region.

The eye has little trajectory movement, and therefore little relative separation, yielding low mixing rates for all measures. The updraft jet has little separation even with

ACPD
9, 18545–18596, 2009

long trajectory flights over short time intervals, and also gives low mixing rates. The highest mixing rates occur at the boundary-layer inflow, where separation from the sea surface and transport of some trajectories into the updraft give a high separation of trajectories. The environment has hyperbolic characteristics as a transition between a single eyewall and a secondary region of convection occurs, but higher mixing rates are not indicative of higher eyewall velocities, but of more hyperbolic mixing characteristics in this region.

While higher velocities are generally associated with higher mixing rates, the presence of hyperbolic structures may allow or inhibit transport, which may precede or trail higher intensities. A lead or lag of mixing rates to velocities is then appropriate to capture the hyperbolic effects. Average mixing rates from the time-dependent velocity field (Tables 3 and 4) are generally between the strong and weak composite wind field mixing rates, which also suggests that extreme values of mixing rates can be related to extreme values of intensity.

8 Time series analysis

The dependence of the mixing rates on the initial time gives time series that can be analyzed to establish correlations between different quantities. The MMR, FMR and RD were all computed for different integration times for the sequence of initial times.

For a quasi steady-state hurricane, the connection between intensity and mixing rates is not obvious, especially when the rates are determined by an integration time that lasts longer than a complete period from high to low maximum winds, where the mixing rate value is assigned to the initial time of integration.

The FMR is fit to an exponential decay function, but the curve of the FTLE distribution function does show a decay for $t - t_0 \leq 10$ min. After 10 min, the FMR can be computed by fitting an exponential decay curve to the remaining data. The optimal integration time varies for each box, and for initial times. The FTLE mixing rate best fits an exponential function at integration times of between 20 and 80 min, which is reasonable since the

ACPD
9, 18545–18596, 2009

FTLE values give a short time measure of advective mixing.

In Antonsen Jr. et al. (1996), the MMR has been compared to the FTLE mixing rates for closed domains in time periodic velocity fields, with the FTLE rate being measured at 10 times higher than the measured mixing rate. By allowing initial trajectories to be dispersed into the domain without exiting the domain, the FMR and MMR can be considered as short time versions of mixing rates within a closed domain. For short time intervals, different initial conditions can lead to significant differences in the mixing rates, as neighboring boxes can show mixing rates differing by a factor of 10. The FMR is within a factor of 2 of the MMR, which is lower than in Antonsen Jr. et al. (1996), and is smaller than the variations of rates with the initial box.

The relative dispersion is similar to the FTLE's for an initial box in that it tracks the cumulative separation of trajectories over an integration time. The relative dispersion is fit to a power law for integration times of 20 min to 120 min. For integration times of 20 min to 60 min, the box representing the boundary layer inflow has superdiffusive mixing as a portion of the initial set is advected into the updraft, while other trajectories become temporarily entrained within finite time hyperbolic manifolds that are in the environment above the inflow. These trajectories soon mix into the updraft, and the rate of dispersion decreases to subdiffusive levels at integration times above 40 min. The reason for the change between the superdiffusive and subdiffusive regime at 60 min is likely that the trajectories in the updraft have reached the upper level outflow jet at this time period. For the other boxes, the mixing is always at subdiffusive levels for this choice of initial boxes.

The differences in mixing rates across different boxes for a variety of integration times indicate that the initial boxes do divide the domain into dynamically distinct regions with different mixing properties. In particular, the eye has relatively small trajectory movements compared to the other regions, and all mixing rates are lower in this region.

The time dependent mixing rates can be tested for corrrelation against each of the extrema of the u, v, and w winds. All of the mixing rates give higher values when there is higher averaged trajectory separation over a time interval of integration, but the

ACPD
9, 18545–18596, 2009

winds are given instantaneously. High particle velocities and velocity gradients at an initial time would indicate high initial separation but may not correlate to high averaged separation, which would then be assigned to the initial time for Lagrangian rates. The structural differences in the strong and weak composite FTLE fields (Fig. 15) indicate that different mixing properties and different structures in the wind fields may coincide with differences in intensity. Correlations of mixing rates to a time lag of maximum winds can indicate the existence of structures which precede or be an effect of higher intensity. Lagrangian structures are an effect of the (u, w)-velocity field from previous times in a forward time integration, or future times in a backward time integration. High or low instantaneous winds cannot be seen as neccessarily showing the structures that exist from the maximal and minimal averaged autonomous fields, due to the unsteady nature of the velocity fields. The instantaneous winds may be related to the effect of Lagrangian structures appearing over a series of initial times.

8.1 Correlation of mixing rates to maximum tangential winds

The maximum tangential winds are taken here as the main indicator of intensity. The azimuthal velocity component is not used for computing trajectories, but is coupled to the radial and vertical velocity component through a system of PDE's. The tangential wind is not periodic, but oscillates between relatively high and relatively low values.

Autocorrelation values of maximal tangential winds for time lags above 6 min are always below .5 (Fig. 16), showing little predictability within the velocity fields. Correlations of maximal wind values of the separate velocity components to each other are even less than .2.

The correlations of mixing rates to maximum tangential winds (some correlations above .7) is far greater than to the extrema of radial (correlations below .5) or vertical (correlations below .4) winds.

The oscillations of the maximum tangential winds occur over a time interval of approximately 20 min. A 40 min integration time is close to the period of two oscillations, and is the maximum integration time that yields significant correlation of mixing rates

ACPD
9, 18545–18596, 2009

to maximum tangential winds. The rates converge to an exponential or power law after a short time interval, and begin to show correlation after an integration time of 10 min. The best fit to the power law for relative dispersion occurs for integration times of 18 to 40 min.

The mixing rates are functions of initial time for each of the six boxes. The different initial boxes give very different mixing rates, with higher mixing rates occuring in the boxes that have the highest velocities. The boundary layer inflow and eyewall updraft boxes show correlation to maximum tangential winds, with the eyewall updraft showing the highest correlation for both forward (Table 5) and backward (Table 6) integration time.

Trajectories can be integrated forward or backward in time, giving Lagrangian fields that show attracting structures (forward integration), or repelling structures (backward integration). For correlating a Lagrangian quantity to intensity, the forward time integration gives Lagrangian fields that result from future velocities, while backward time integration gives fields that result from past velocities. The wind field at an initial time is predicted by the backward time field at that time, and predicts the forward time field at that initial time. Backward time integration showed higher correlation with the wind fields than forward time integration for most boxes with high correlation.

Correlating the Lagrangian fields to a time lag of the velocity field shows how the Lagrangian structures and maximum winds are predictive of each other. Predicting hurricane intensity (on admittedly very short time scales) by mixing rates can be accomplished by showing a correlation between a backward time integrated Lagrangian mixing rate lagged against the maximum winds, since a function of previous information would correlate to future information.

RD and FRD show similar high correlation to maximum tangential winds, suggesting that both quantities are similar for predictability. The correlation for both measures is higher for a backward time integration and for the Lagrangian field lagged against the maximum wind, which suggests that the Lagrangian measures are predictive of the maximum winds. Higher separation and mixing rates backward in time from the eyewall

ACPD
9, 18545–18596, 2009

updraft are caused from a larger source of material that enters the updraft forward in time. The structures that are repelling backward in time are attracting forward in time, thus the higher mixing rates are likely also due to the presence of a stronger updraft jet. The autonomous field from the highest averaged velocities shows a very strong updraft jet, while the low velocities show a weaker updraft jet that is not as efficient in advecting all entering trajectories into the outflow.

Though RD and the FRD produce similar correlations to maximal tangential winds, especially for backward time integrations from the eyewall updraft, the RD gives slightly stronger results. This shows that total separation is important, and using the separation in the direction of maximal exapnsion does not give any additional advantage. Though the relative dispersion has higher correlation to maximal winds, the FTLE fields still have the advantage of studying the entrainment of trajectories, and viewing LCS's. Both measures show a higher correlation at 20 min and the correlation begins to diminish at an integration time of 40 min. The RD is useful for both forward and backward time integration (Figs. 17 and 19), while the FRD is useful only for backward time integration (Figs. 18 and 19). The MMR does not show correlation as high as the other rates, but shows some correlation for the shortest integration time of 20 min (Fig. 18). The MMR is dependent on the final position of trajectories, and not only on the separation of trajectories. Over longer integration times, this could make the MMR more sensitive to movement caused by gravity waves.

The FRD shows negative correlation of −.6684 to maximal inflow winds for the boundary layer inflow box with a forward time integration of 20 min and a 4 min time lag, which shows that enhanced mixing is correlated with the enhancement of the BL inflow (a negative of the extreme minimum of the u field). The boundary layer inflow has more hyperbolic mixing characteristics than the other regions, which may make FTLE's better suited as a mixing measure in this region. This is the only region where the FRD shows higher correlation than the RD. The eywall updraft box also shows negative correlation from FTLEs with a forward time integration.

In many cases, the correlation improved when the Lagrangian rates were lagged

ACPD
9, 18545–18596, 2009

against the maximum winds. The Lagrangian structures are then predictive of maximum tangential winds. Correlation of 0.6 or higher is present for a lag of up to 10 min, which is about half of a period of oscillation of the maximum tangential winds. The highest correlations occur for 2 to 6 min lags, which means that the initial time of integration for the Lagrangian fields is at a time where the maximum tangential winds are increasing, but before the local maximum occurs.

9 Conclusions

Lagrangian mixing for the complex velocity fields of an axisymmetric hurricane of Rotunno and Emanuel (1987) has been studied. The inner core region was shown to have Lagrangian structures that vary over time, and play a prominent role for mixing in the region, which is related to hurricane intensity. We have produced mixing rates that correlate to maximum winds, and can be used for a short time prediction of the maximum winds. The mixing rates computed in our study are an extension of mixing rates established for closed regions and steady or time-periodic velocity fields, which have been adapted to the spatial and temporal complexities of the model. In particular, our rates depend on initial time, integration time, time lag, and two spatial coordinates. Various measures of maximal Eularian intensity have been extracted from the u, w, and v wind fields, and compared to the time-dependent mixing rates. A correlation analysis showed that the rates have highest correlation to the maximum tangential winds. The conclusions drawn are that episodes of enhanced mixing between the low-level eye and eyewall precede short-time enhancements of intensity, and thus favor the interpretation that new local generation of buoyancy at the eyewall lead to enhanced thermodynamic cycling of the hurricane heat engine. In principle, the mixing could have been responsive of short-term fluctuations of intensity in response to enhanced flow gradients, or mixing could have directly spun down tangential winds through angular momentum mixing, but since mixing precedes such episodes, neither of these explanations can be favored by the present results. Further work will use a canonical correlation analysis to

ACPD
9, 18545–18596, 2009

find correlations between the mixing rates as well as the maximal winds. The methods presented here will also be extended to a three-dimensional hurricane model.

Acknowledgements. This work was supported by NSF Cooperative Agreement ATM-0715426. We thank W. Schubert, E. Hendricks, A. Jamshidi, K. Musgrave, C. Rozoff, J. Vigh, and M. Riemer for their discussions.

References

Atonsen Jr., T. M.,Fan, Z., Ott, E., and Garcia-Lopez, E.: The role of chaotic orbits in the determination of power spectra of passive scalars, Phys. Fluids, 8, 3094–3104, 1996. 18547, 18553, 18564

Braun, S. A.: A cloud-resolving simulation of Hurricane Bob (1991): Storm structure and eyewall buoyancy, Mon. Weather Rev., 130, 1573–1592, 2002. 18546

Cram, T. A., Persing, J., Montgomery, M. T., and Braun, S. A.: A Lagrangian trajectory view on transport and mixing processes between the eye, eyewall, and environment using a high resolution simulation of hurricane Bonnie (1998), J. Atmos. Sci., 64, 1835–1856, 2007. 18546

Frank, W. M. and Ritchie, E. A.: Effects of environmental flow upon tropical cyclone structure, Mon. Weather Rev., 127, 2044–2061, 1999. 18546

Frank, W. M. and Ritchie, E. A.: Effects of vertical wind shear on the intensity and structure of numerically simulated hurricanes., Mon. Weather Rev., 129, 2249–2269, 2001. 18546

Green, M. A., Rowley, C. W., and Haller, G.: Detection of Lagrangian Coherent Structures in 3D Turbulence, J. Fluid Mech., 2006. 18547, 18550

Haller, G.: Finding finite-time invariant manifolds in two-dimensioanl velocity fields, Chaos, 10, 99–108, 2000. 18547

Haller, G.: Lagrangian coherent structures from approximate velocity data, Phys. Fluids, 14, 1851–1861, 2002. 18547, 18550

Haller, G.: Exact theory of unsteady separation for two-dimensional flows, J. Fluid Mech., 512, 257–311, 2004. 18547

Haller, G. and Poje, A.: Finite time transport in aperiodic flows, Physica D, 119, 352–380, 1997. 18547, 18550

Haller, G. and Yuan, G.: Lagrangian coherent structures and mixing in two-dimensional turbulence, Physica D, 147, 352–370, 2000. 18547, 18550

Huber, M., McWilliams, J. C., and Ghil, M.: A climatology of turbulent dispersion in the troposphere, J. Atmos. Sci., 58, 2377–2394, 2001. 18547, 18550, 18554, 18555
Kossin, J. P. and Eastin, M. D.: Two distinct regimes in the kinematic and thermodynamic structure of the hurricane eyewall, J. Atmos. Sci., 58, 1079–1090, 2001. 18546
Kossin, J. P. and Schubert, W. H.: Mesovortices, polygonal flow patterns, and rapid pressure falls in hurricane-like vortices, J. Atmos. Sci., 58, 2196–2209, 2001. 18546
Liu, Y., Zhang, D. L., and Yau, M. K.: A multiscale numerical study of Hurricane Andrew (1992), Part V: Inner core thermodynamics, Mon. Weather Rev., 130, 2745–2763, 2002. 18546
Montgomery, M. T., Bell, M. M., Aberson, S. D., and Black, M. L.: Hurricane Isabel (2003): New insights into the physics of intense storms, Part I: Mean vortex structure and maximum intensity estimates., B. Am. Meteorol. Soc., 87, 1349–1354, 2006. 18546
Persing, J. and Montgomery, M. T.: Hurricane superintensity, J. Atmos. Sci., 60, 2349–2371, 2003. 18546, 18556
Roll, H.: Physics of the marine atmosphere, Academic Press, 1965. 18556
Rotunno, R. and Emanuel, K.: An air-sea interaction theory for tropical cyclones, Part II: evolutionary study using a nonhydrostatic axisymmetric numerical model, J. Atmos. Sci., 44, 542–561, 1987. 18547, 18548, 18556, 18568
Rutherford, B., Persing, J., Dangelmayr, G., Schubert, W. H., and Montgomery, M. T.: Advective mixing in a nondivergent barotropic hurricane model, preprint, submitted for publication, 2009. 18547
Schubert, W. H., Montgomery, M.'T., Taft, R. K., Guinn, T. A., Fulton, S. R., Kossin, J. P., and Edwards, J. P.: Polygonal eyewalls, asymmetric eye contraction, and potential vorticity mixing in hurricanes, J. Atmos. Sci., 56, 1197–1223, 1999. 18546
Shadden, S. C., Lekein, F., and Marsden, J. E.: Definition and properties of Lagrangian coherent structures from finite-time Lyapunov exponents in two-dimensional aperiodic flows, Physica D, 212, 271–304, 2005. 18552, 18553
Smagorinsky, J.: General circulation experiments with the primitive equation, I: The basic experiment, Mon. Weather Rev., 91, 99–164, 1963. 18556
Smith, R. K., Montgomery, M. T. and Zhu, H.: Buoyancy in tropical cyclones and other rapidly rotating atmospheric vortices, Dynam. Atmos. Oceans, 40, 189–208, 2005. 18546
Surana, A. and Haller, G.: Ghost manifolds in slow-fast systems, with applications to unsteady fluid flow separation, Physica D, 237, 1507–1529, 2008. 18547
Voth, G. A., Saint, T. C., Dobler, G., and Gollub, J. P.: Mixing rates and symmetry breaking

in two-dimensional chaotic flow, Phys. Fluids, 15, 2560–2566, 2003. 18547, 18550, 18551, 18554
Willoughby, H. E.: Tropical cyclone eye thermodynamics, Mon. Weather Rev., 126, 3053–3067, 2001. 18546

Table 1. Mixing rates of strong composite (top) and weak composite (bottom) velocity field for six initial boxes with 20 min forward integration time.

	FMR	FRD	MMR	RD
low-level eye	.0488	.0224	.0264	.1683
low-level eyewall	.0638	.1288	.0811	.1852
BL inflow	.0878	1.147	.2183	.5303
eye	.0878	.0267	.0369	.1655
eyewall updraft	.0479	.0200	.0609	.1700
environment	.0641	.0884	.2284	.0097
low-level eye	.0553	.0400	.0181	.1666
low-level eyewall	.0718	.1567	.0482	.1833
BL inflow	.0770	.6421	.1849	.2837
eye	.0460	.0175	.0294	.1692
eyewall updraft	.0519	.0279	.0509	.1750
environment	.0629	.0930	.1380	.2621

Table 2. Mixing rates of strong composite (top) and weak composite (bottom) velocity field for the six initial boxes with 40 min forward integration time.

	FMR	FRD	MMR	RD
low-level eye	.0281	.0135	.0209	.1406
low-level eyewall	.1361	.1288	.0625	.1996
BL inflow	.0574	16.33	.1277	.2929
eye	.0286	.0184	.0322	.1368
eyewall updraft	.0274	.0103	.0466	.1452
environment	.0381	.3446	.0841	.3084
low-level eye	.0329	.0359	.0113	.1367
low-level eyewall	.0421	.1792	.0492	.1867
BL inflow	.0499	2.295	.1080	.8242
eye	.0262	.0089	.0265	.1435
eyewall updraft	.0307	.0201	.0517	.1589
environment	.0360	.3275	.0945	.4513

ACPD
9, 18545–18596, 2009

Table 3. Average mixing rates of time-dependent velocity field for the six initial boxes with 20 min forward integration time.

	FMR	FRD	MMR	RD
low-level eye	.0481	.0219	.0147	.1670
low-level eyewall	.0578	.0686	.0557	.1752
BL inflow	.0793	.9454	.1897	.3357
eye	.0450	.0177	.0264	.1675
eyewall updraft	.0469	.0199	.0392	.1685
environment	.0569	.0674	.0803	.1967

ACPD
9, 18545–18596, 2009

Table 4. Average mixing rates of time-dependent velocity field for the six initial boxes with 40 min forward integration time.

	FMR	FRD	MMR	RD
low-level eye	.0259	.0069	.0044	.1354
low-level eyewall	.0321	.0505	.0352	.1567
BL inflow	.0483	4.313	.1069	.9872
eye	.0237	.0040	.0060	.1381
eyewall updraft	.0038	.0199	.0121	.1368
environment	.0307	.1182	.0523	.2162

ACPD
9, 18545–18596, 2009

Table 5. Correlation coefficients of the forward time mixing rates time series for the eyewall updraft box to the maximum tangential winds time series for integration calculated over the time range 400–800 min, during the quasi-steady state phase of the velocity fields. The mixing rates are computed for 20, 30, and 40 min integration times, and are lagged by 0, 2, 4, 6, 8, and 10 min behind the winds.

	FTLE	RD	MMR
20 min	.0249	.6397	−.2869
2 min lag	.0391	.6892	−.1482
4 min lag	.0408	.6736	.0314
6 min lag	.0423	.5991	.2283
8 min lag	.0554	.4775	.4159
10 min lag	.0870	.3238	.5707
30 min	.1686	.4950	−.3534
2 min lag	.1831	.5821	−.3825
4 min lag	.1808	.6166	−.3715
6 min lag	.1717	.6010	−.3187
8 min lag	.1670	.5419	−.2249
10 min lag	.1749	.4473	−.0919
40 min	.1033	.4315	−.0639
2 min lag	.1381	.5118	−.1023
4 min lag	.1547	.5634	−.1335
6 min lag	.1602	.5706	−.1586
8 min lag	.1613	.5404	−.1787
10 min lag	.1620	.4812	−.1898

ACPD
9, 18545–18596, 2009

Table 6. Correlation coefficients of the backward time mixing rates time series for the eyewall updraft box to the maximum tangential winds time series for integration calculated over the time range 400–800 min, during the quasi-steady state phase of the velocity fields. The mixing rates are computed for 20, 30, and 40 min integration times, and are lagged by 0, 2, 4, 6, 8, and 10 min behind the winds.

	FTLE	RD	MMR
20 min	.4520	.5895	.2343
2 min lag	.6079	.7049	.4140
4 min lag	.7061	.7499	.5549
6 min lag	.7354	.7209	.6407
8 min lag	.6965	.6258	.6632
10 min lag	.6007	.4814	.6226
30 min	.4919	.4725	−.2744
2 min lag	.6053	.6301	−.1370
4 min lag	.6660	.7279	.0302
6 min lag	.6673	.7563	.2702
8 min lag	.6098	.7161	.3720
10 min lag	.5011	.6178	.5096
40 min	.4967	.3982	−.3772
2 min lag	.5724	.5717	−.3574
4 min lag	.5993	.6917	−.3013
6 min lag	.5773	.7451	−.2117
8 min lag	.5114	.7295	−.0914
10 min lag	.4076	.6527	.0514

ACPD
9, 18545–18596, 2009

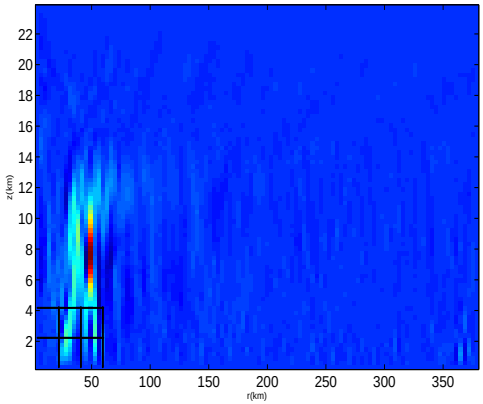

(a)

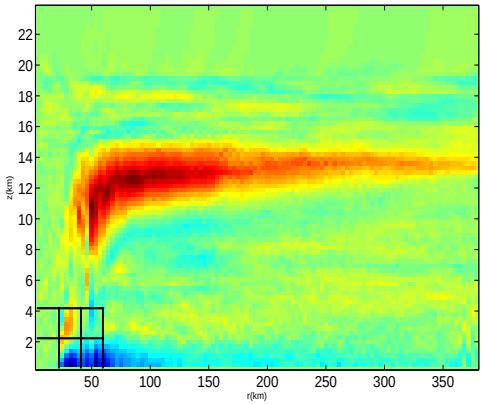

(b)

Fig. 1. Single time slice of the radial velocity field **(a)** and vertical velocity field **(b)** with boxes used for computing mixing rates in the lower left of each image.

ACPD

9, 18545–18596, 2009

Lagrangian mixing in an axisymmetric hurricane model

B. Rutherford et al.

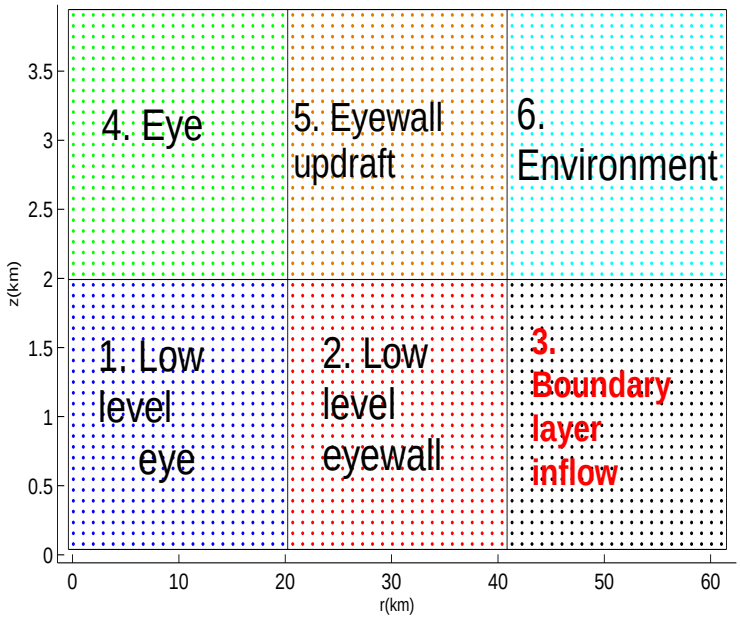

Fig. 2. Boxes in the lower inner core with initial trajectory positions.

ACPD
9, 18545–18596, 2009

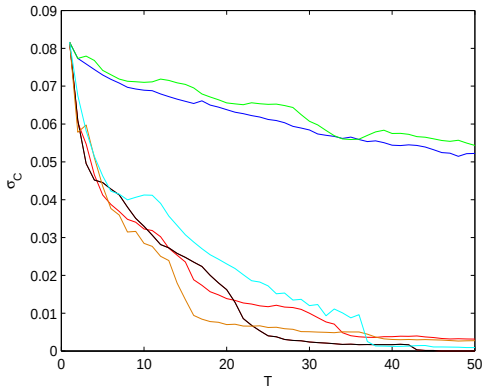

(a)

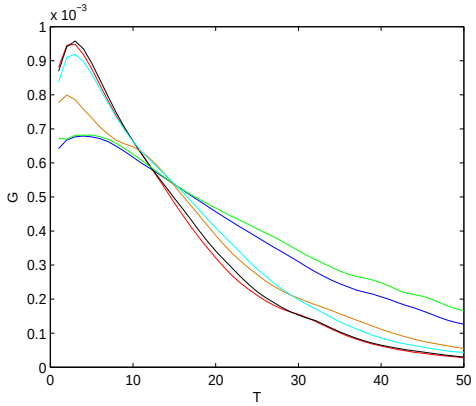

(b)

Fig. 3. Concentration variance $\sigma_c(t, t_0)$ **(a)** and FTLE distrbution function $G(t, t_0)$ **(b)** plotted versus integration time T for the 6 mixing boxes with trajectories seeded t_0=400 min. Other initial times give similar decay structure but different quantitative details.

ACPD

9, 18545–18596, 2009

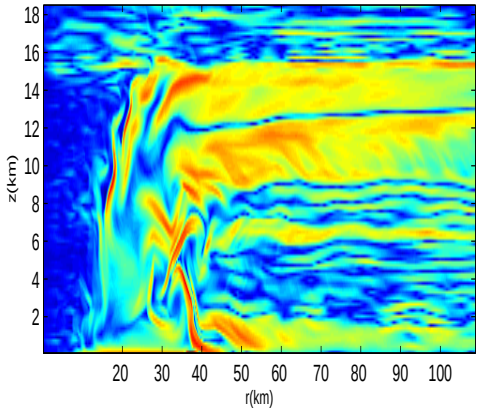

Fig. 4. Forward **(a)** and backward **(b)** time FTLE fields integrated 20 min with an initial time of 400 min.

ACPD
9, 18545–18596, 2009

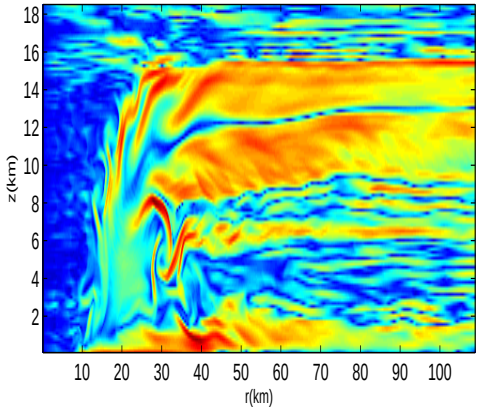

Fig. 5. Forward **(a)** and backward **(b)** time FTLE fields integrated 20 min with an initial time of 420 min.

ACPD
9, 18545–18596, 2009

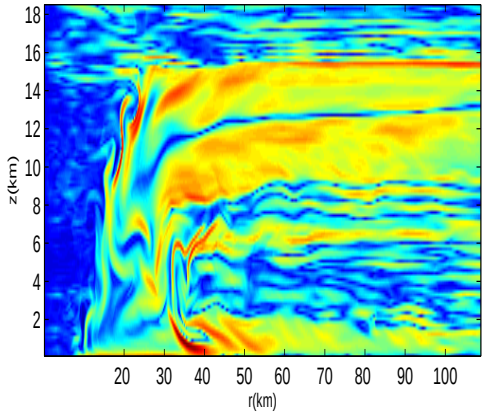

Fig. 6. Forward **(a)** and backward **(b)** time FTLE fields integrated 20 min with an initial time of 440 min.

ACPD
9, 18545–18596, 2009

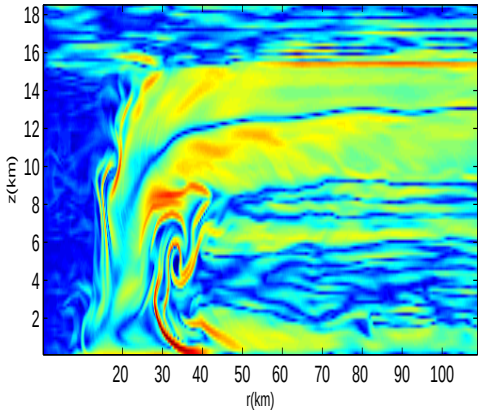

Fig. 7. Forward **(a)** and backward **(b)** time FTLE fields integrated 20 min with an initial time of 460 min.

ACPD
9, 18545–18596, 2009

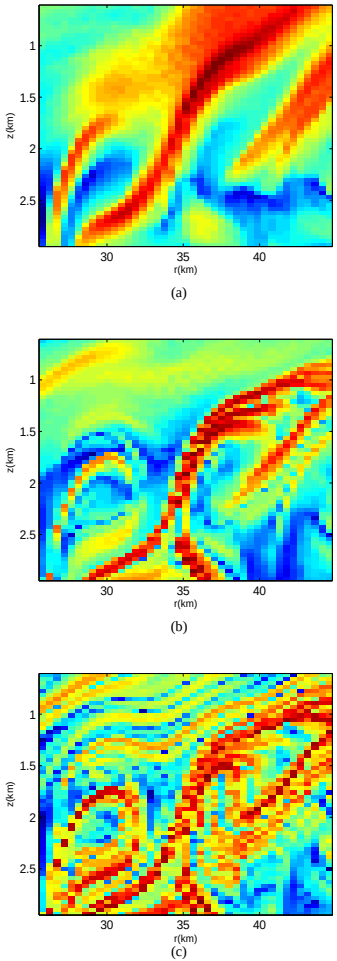

Fig. 8. Ridge of forward time FTLE field at initial time of 400 min integrated 20 **(a)**, 60 **(b)**, and 120 **(c)** min.

ACPD

9, 18545–18596, 2009


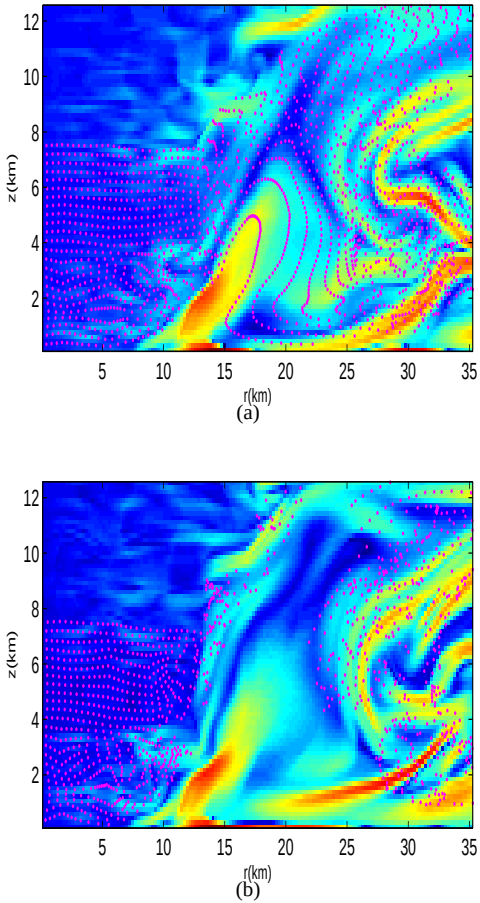

Fig. 9. Backward time FTLE field integrated $T=-20$ min for initial times of $t_0=420$ min **(a)** and $t_0=460$ min **(b)**. The red dots mark the positions at time $t=t_0$ of trajectories seeded on a uniform grid at $t_0=400$ min.

ACPD
9, 18545–18596, 2009

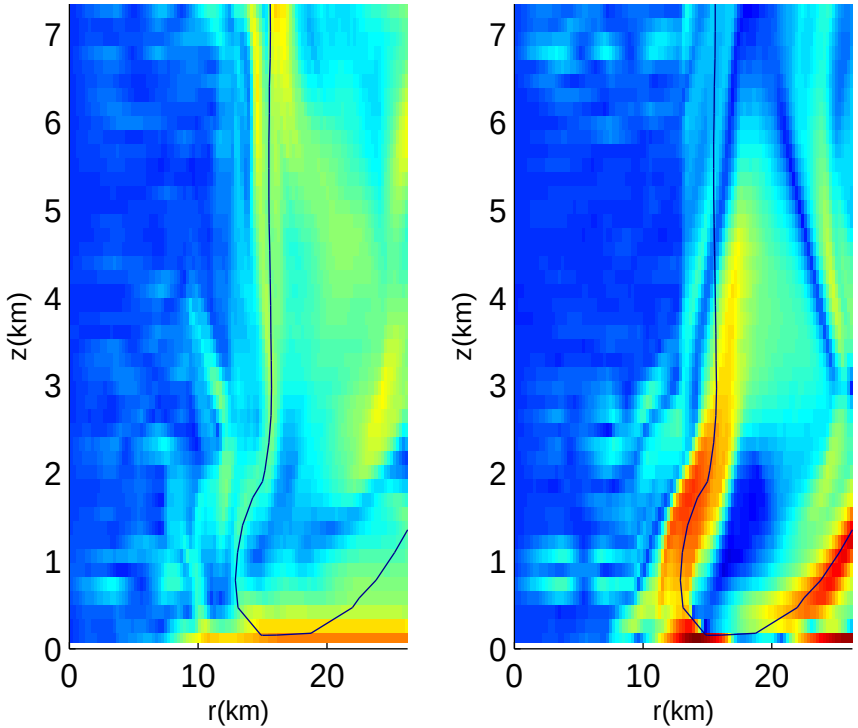

Fig. 10. Forward and backward time FTLE fields at t_0=400 min with 1 m/s vertical wind contour

ACPD
9, 18545–18596, 2009

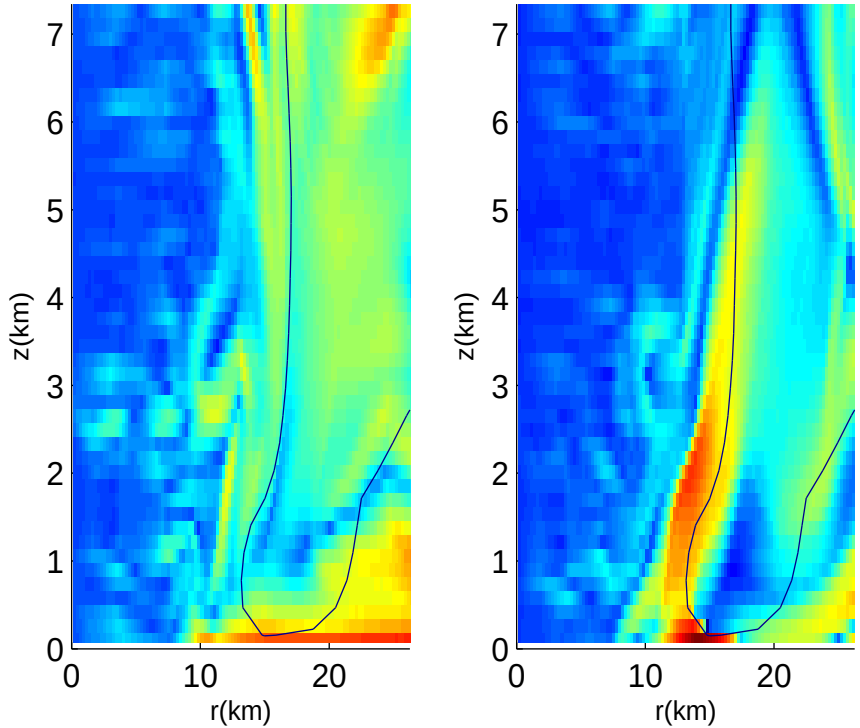

Fig. 11. Forward and backward time FTLE fields at t_0=420 min with 1 m/s vertical wind contour.

ACPD
9, 18545–18596, 2009

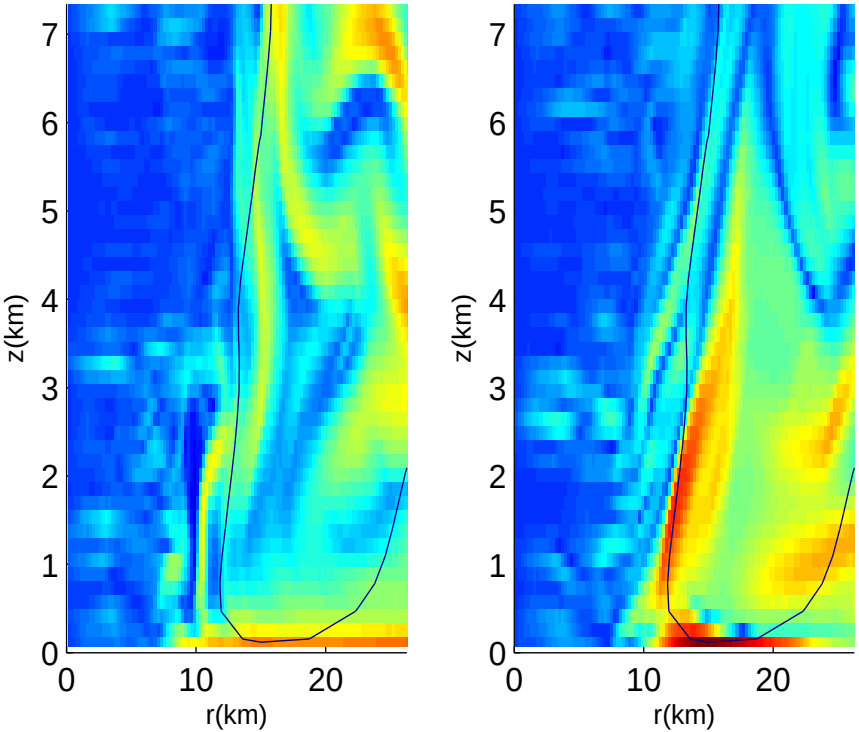

Fig. 12. Forward and backward time FTLE fields at t_0=440 min with 1 m/s vertical wind contour.

ACPD
9, 18545–18596, 2009

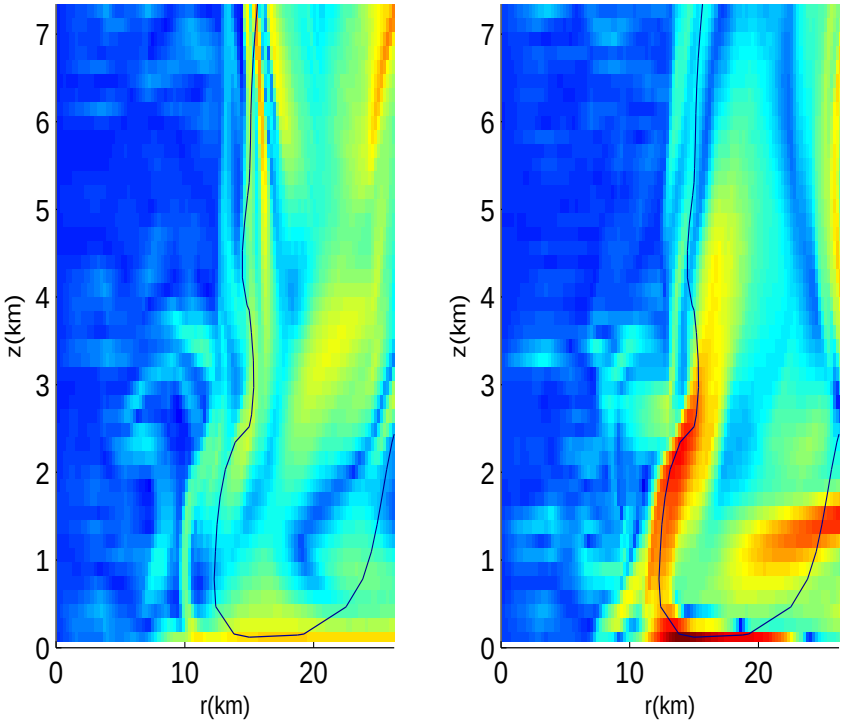

Fig. 13. Forward and backward time FTLE fields at t_0=460 min with 1 m/s vertical wind contour.

ACPD
9, 18545–18596, 2009

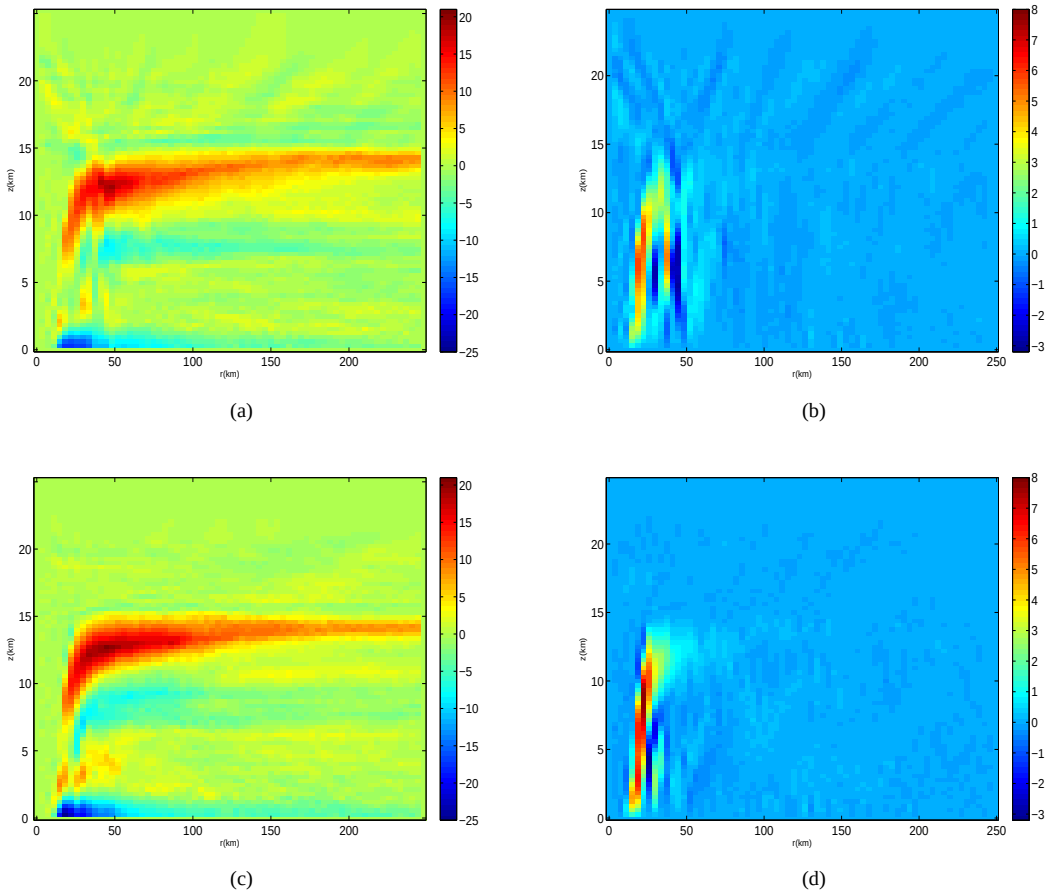

Fig. 14. Weak composite radial **(a)** and vertical **(b)** velocity fields, and strong composite radial **(c)** and vertical **(d)** velocity fields.

ACPD
9, 18545–18596, 2009

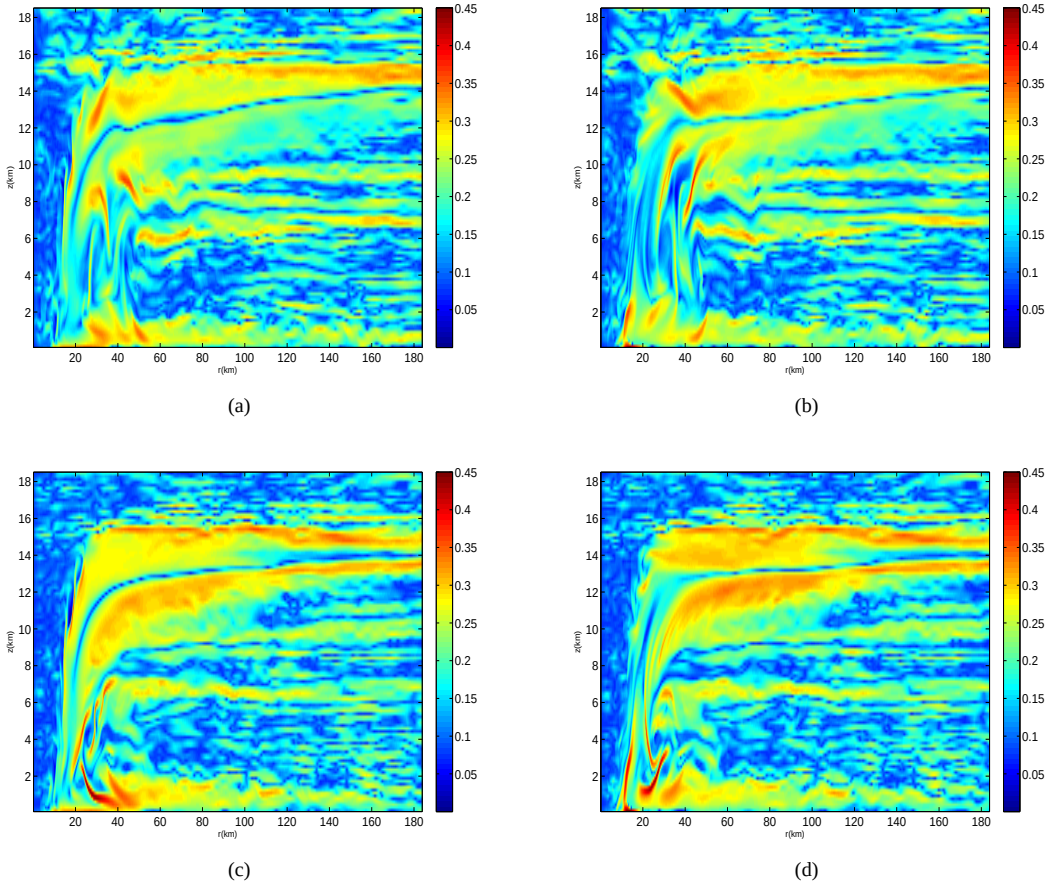

Fig. 15. Weak composite forward **(a)** and backward **(b)** FTLE fields, and strong composite forward **(c)** and backward **(d)** FTLE fields, integrated for 20 min.

ACPD
9, 18545–18596, 2009

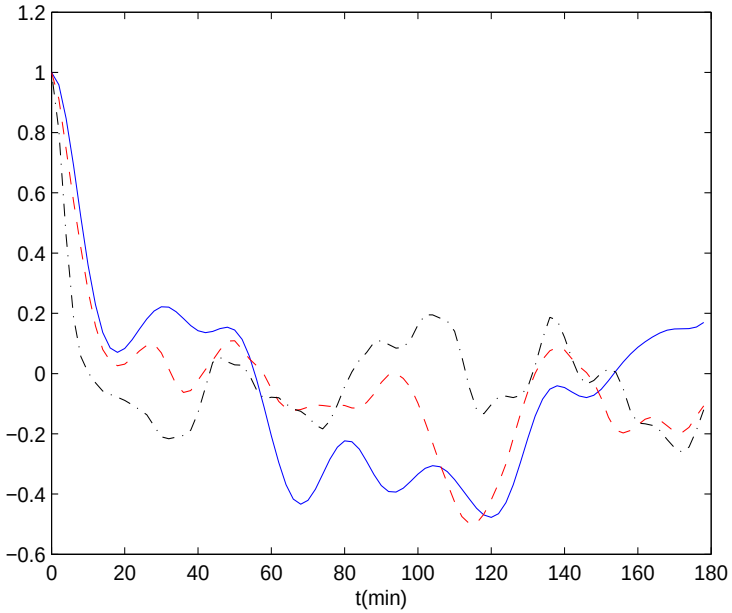

Fig. 16. Autocorrelations of maximal tangential winds (blue), maximal outflow winds (red), and maximal updraft winds (black).

ACPD

9, 18545–18596, 2009

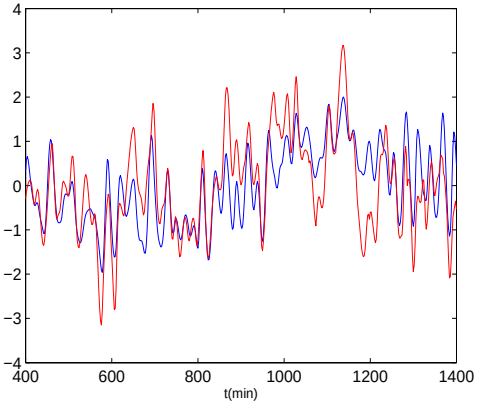

(a)

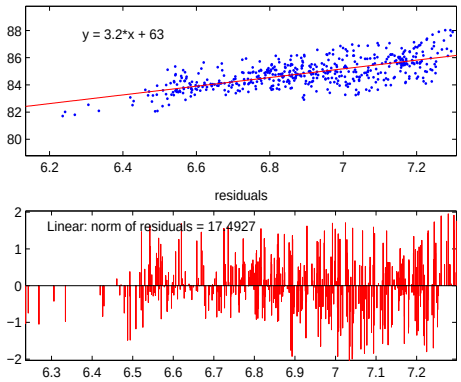

(b)

Fig. 17. **(a)** Normalized relative dispersion for 20 min backward integration (blue), and maximum tangential winds delayed 4 min (red). **(b)** Relative dispersion for 20 min backward integration time against maximum tangential winds, with linear best fit and norm of residuals.

ACPD

9, 18545–18596, 2009

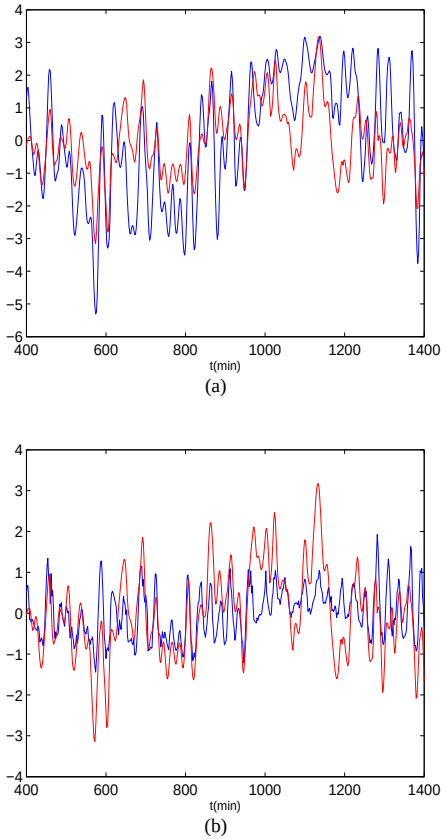

Fig. 18. **(a)** Normalized FTLE measure of relative dispersion for 20 min backward integration (blue), and maximum tangential winds delayed 6 min (red). **(b)** Normalized meaured mixing rate for 20 min backward integration (blue), and maximum tangential winds delayed 8 min (red).

ACPD
9, 18545–18596, 2009

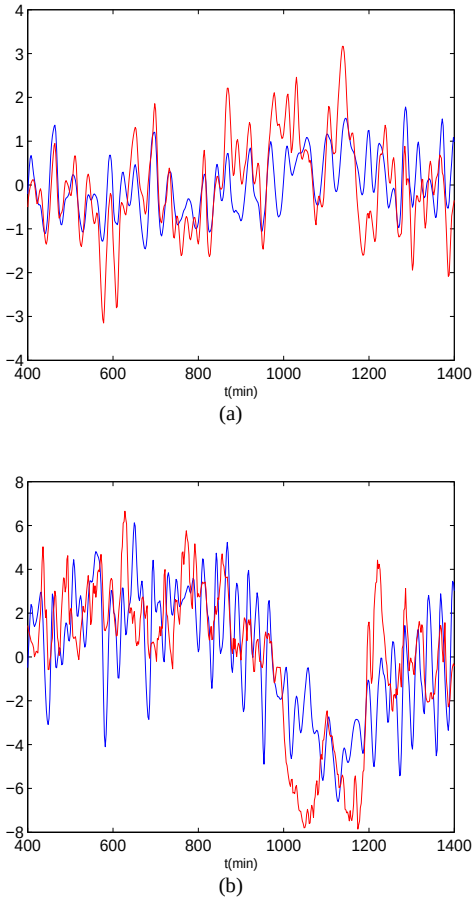

Fig. 19. (a) Normalized relative dispersion for 20 min forward integration (blue), and maximum tangential winds delayed 2 min (red). **(b)** Normalized FTLE measure of relative dispersion for 20 min backward integration (blue), and maximum radial winds delayed 4 min (red).

ACPD

9, 18545–18596, 2009